RSC Advances

PAPER

View Article Online
View Journal | View Issue

Check for updates

Cite this: *RSC Adv.*, 2022, **12**, 12760

The optimization effect of different parameters on the super hydrophobicity of prickly-shaped carbonyl iron particles†

Y. Rabbani,[a] M. Shariaty-Niassar *[a] and S. A. Seyyed Ebrahimi [b]

In this study, the effects of glucose concentration, temperature, and time parameters of the hydrothermal reaction on the growth of prickly-shaped carbonyl iron were studied by using an experimental design to obtain the maximum superhydrophobicity of the magnetic particles. The experimental design was carried out by Response Surface Methodology (RSM) analysis using the Central Composite Design (CCD) method. Field Emission Scanning Electron Microscopy (FESEM) analysis was performed to qualitatively assess the growth of the prickly-shaped carbonyl iron, and Water Contact Angle (WCA) analysis was used to quantify the superhydrophobicity of the resulting particles. The results revealed that the elevation of the concentration and time increased the roughness (prickly shape) of the particle surface and contact angle up to a point, after which it did not affect them. The temperature elevation caused an increase in the prickly shape of the particles and contact angles and then reduced them. The optimum concentration, temperature, and time were 0.75 Mol L^{-1}, 170 °C, and 4 hours, respectively, for the maximum growth of prickly-shaped particles and the maximum contact angle was 169.7°. Fourier-Transform Infrared Spectroscopy (FT-IR) and thermogravimetric analysis (TGA) results confirmed the presence of glucose and stearic acid chemically bonded to the carbonyl iron particles. The X-ray Diffraction (XRD) results showed that the carbonyl iron had been not converted into iron oxide during the synthesis procedures of the superhydrophobic particles. Vibrating Sample Magnetometer (VSM) analysis showed that making the particles superhydrophobic had little effect on the magnetization reduction.

Received 24th December 2021
Accepted 22nd March 2022

DOI: 10.1039/d1ra09334g

rsc.li/rsc-advances

Open Access Article. Published on 26 April 2022. Downloaded on 5/31/2026 3:32:46 PM.
This article is licensed under a Creative Commons Attribution-NonCommercial 3.0 Unported Licence.

1. Introduction

Nowadays, with the development of different industries and the rapid increase in the population, the amount of produced wastewater has increased dramatically. Industrial wastewater discharge, as well as oil spills in seas, rivers, and other vast water resources not only threaten the ecosystems and human health, but also destroy a wide spectrum of natural resources on the Earth, all of which have encouraged researchers to come up with constructive, drastic, and solution-oriented methods to mitigate this kind of serious environmental problem. Some industries that are directly or indirectly related to oil and lubricants commonly use different viable methods for oil/water separation on different scales.[1–3] The common method for oil and water separation is filtration adsorption, which can be conducted by different strategies and materials from the macro- to the nano-scale. Numerous materials with different properties have been produced so far by several strategies such as electrodeposition, photolithography, chemical vapor deposition, colloidal assembly, and electro-spinning. Since almost all of the separation processes are profoundly influenced by interfacial characteristics, synthesized materials for separation should meet the required surface features, such as excellent wettability or superhydrophobicity, large area, good durability, *etc.*[4–8]

In these situations, porous materials such as sponges,[9] foams,[10] and textiles are applied in oil adsorption but these materials suffer from poor selectivity, non-recovery, low efficiency, and low adsorption capacity. The utilization of magnetic particles is one of the favored strategies for oil adsorption from oil-water mixtures due to their cost-effective and fast recovery, low toxicity, and availability.[11,12]

Micronanostructures with magnetic and superhydrophobic properties are dispersed in spilled oil layers. The superhydrophobicity of the particles makes them a suitable adsorbent to selectively adsorb oil, and their magnetization properties lead to their easy collection by a strong magnet. Thus, these modified particles with low cost and stable magnetization capability can be used as efficient and easy-to-

[a]*Transport Phenomena & Nanotechnology (TPNT) Lab., School of Chemical Engineering, College of Engineering, University of Tehran, Tehran 111554563, Iran. E-mail: mshariat@ut.ac.ir*

[b]*Advanced Magnetic Materials Research Center, School of Metallurgy and Materials, College of Engineering, University of Tehran, Tehran 111554563, Iran*

† Electronic supplementary information (ESI) available. See https://doi.org/10.1039/d1ra09334g

© 2022 The Author(s). Published by the Royal Society of Chemistry

Open Access Article. Published on 26 April 2022. Downloaded on 5/31/2026 3:32:46 PM.
This article is licensed under a Creative Commons Attribution-NonCommercial 3.0 Unported Licence.

control oil adsorbents for separating oil from complex multiphase mixtures.[13,14] Superhydrophobic surfaces, which have a contact angle of higher than 150°, are among the most effective options for oil and water separations, which are typically used in the form of particles,[15] porous,[16] membrane,[17,18] or mesh materials.[19,20] Various studies have been conducted to improve the capacity of oil-water adsorption.[21–24]

Simmons *et al.*[25] studied oil separation by magnetic nanoparticles in the oily wastewater treatment industry. Doan *et al.*[26] suggested a simple approach for surfactant-free and surfactant-stabilized structures to separate the oil-water mixture and emulsions by superhydrophobic/superoleophobic iron particles. They found that these particles have a WCA above 160° and separation efficiency above 99.9%. Zhou *et al.*[27] developed Fe_2O_3@C magnetic nanoparticles with high oil adsorption selectivity. They showed that these particles were highly hydrophobic with a WCA of 162.9° and could be recycled in water-oil separation for four cycles with a low decline in water contact angle.

High magnetic saturation, high magnetic permeability, and reversible behavior, as well as good stability in a varied range of temperatures, are the features that make the carbonyl iron particles a potential tool for oil adsorption in the oil spillage process.[28–30] A few studies have been made on the modification of carbonyl iron particles to separate oil from water. Duan *et al.*[31] studied the effect of superhydrophobic/superoleophobic carbonyl iron particles on the removal of organic pollutants, where the surface of the carbonyl iron was modified with copper. They showed that the water contact angle was between 140 and 164°, with adsorption efficiency above 99.9%. Another study was conducted to show the mechanism of carbonyl iron magnetic particles for Pickering emulsions in the presence of a magnetic field.[32]

In this research, in order to obtain the maximum superhydrophobicity of the magnetic particles, the effects of glucose concentration, reaction temperature, and reaction time parameters have been optimized in the hydrothermal synthesis of carbonyl iron particles with stearic acid and glucose. Therefore, first, the experimental design was performed with Design-Expert software to achieve maximum hydrophobicity. Secondly, the qualitative evaluation of the growth of these prickly shapes was done by FESEM analysis, while WCA analysis was performed for the quantitative evaluation of the superhydrophobicity of the particles. Finally, the optimum superhydrophobic particles were characterized by FESEM, FT-IR, TGA, XRD, and VSM.

2. Experimental method

2.1 Materials

Carbonyl iron particles (BASF Company, Germany) (CI) were used as the magnetic core, along with glucose (G), and stearic acid (SA) (Sigma-Aldrich, Germany) as the hydrophobic material. Acetone, toluene, and ethanol were provided by Merck Company. In this paper, the @ symbol shows the chemical bond.

2.2 Synthesis of carbonyl iron with glucose (CI@G)

Carbonyl iron particles (5 g) were dispersed in ethanol and then sonicated for about 40 minutes, after which it was washed three times with ethanol and deionized water. Glucose solution (50 ml of C molar) was added and irradiated for about 40 minutes by an ultrasonic probe, deoxygenated with nitrogen, and located for t (1 : 4 hour) hours at temperature T (160–200 °C) in an autoclave (these parameters were optimized by the Design-Expert software). Ethanol, toluene, and acetone were used to wash the product three times. Finally, the magnetic particles were collected and dried for 4 hours at 60 °C in an oven.

2.3 Modification of CI@G with stearic acid (CI@G@SA)

Here, 2 g of glucose-modified carbonyl iron particles were combined with toluene and agitated for 20 minutes. Next, 0.2 g (10 w%) stearic acid was dissolved in toluene (10 mL) and agitated for 20 minutes before being added to the carbonyl iron solution. At 75 °C, the resultant mixture was agitated for 4 hours under nitrogen gas, and then ethanol, toluene, and acetone were used to wash the product three times. After that, the magnetic particles were collected using magnetic equipment and dried for 4 hours at 60 °C in an oven.

2.4 Experimental design method

Response Surface Methodology (RSM) analysis is a mathematical and statistical method for process modeling and

Table 1 Central Composite Design for all variables obtained from the Design-Expert software

	Range and levels				
Independent variables	−2	−1	0	1	2
Concentration of glucose (C, %)	0	0.25	0.5	0.75	1
Temperature of reaction (T, °C)	160	170	180	190	200
Time of reaction (t, hour)	1	2	3	4	5

	Experimental design		
Run	Temperature (°C)	Concentration (Mol L^{-1})	Time (hour)
1	160	0.5	3
2	170	0.25	2
3	170	0.25	4
4	170	0.75	2
5	170	0.75	4
6	180	0	3
7–12	180	0.5	3
13	180	0.5	1
14	180	0.5	5
15	180	1	3
16	190	0.25	2
17	190	0.25	4
18	190	0.75	2
19	190	0.75	4
20	200	0.5	3

Open Access Article. Published on 26 April 2022. Downloaded on 5/31/2026 3:32:46 PM.
This article is licensed under a Creative Commons Attribution-NonCommercial 3.0 Unported Licence.

optimization. This method is especially useful when the effects of multiple independent variables are evaluated simultaneously. In this research, the independent variables included the concentration of glucose (C), reaction temperature (T), and reaction time (t), which were used for examining WCA measurements. The level and range of variables in a coded and decoded manner are presented in Table 1. The independent variables' values were considered by a five-level experimental method and assigning the lowest value of -2 and maximum value of 2 in the full Central Composite Design (CCD) of RSM *via* the Design-Expert (Ver.11) software. As can be seen in Table 1, 20 tests including 8 factorial points with 6 axial points and 6 replications in the central point were selected to study the effects of several parameters such as time, temperature, glucose, and concentration on the hydrothermal reaction efficiency and, thus, WCA.

Water Contact Angle (WCA or Y) and operational parameters were defined by the following equation.

$$Y = \alpha_0 + \sum_{i=1}^{5} \alpha_i X_i + \sum_{i=1}^{5} \alpha_{ii} X_i^2 + \sum_{i=1}^{4} \sum_{j=i+1}^{5} \alpha_{ij} X_i X_j + \varepsilon \qquad (1)$$

Y denotes the predicted response (% predicted WCA), and X_i, X_j are the independent variables. The α_i were defined as linear effects, α_{ii} as quadratic effects, α_{ij} as binary interactions, and ε as the estimation coefficient effects on the response. Coefficients in eqn (1) were achieved from the Analysis of Variance (ANOVA). The values of F and P determined the degree of importance of the model parameters. The F-Test was used for comparing model variance with residual variance. The P-value was used to determine the possibility of the null hypothesis being true. In this regard, the model term is significant if the P-value is less than 0.05 and has a meaningful effect on the response. Finally, the individual and interaction effects of variables were visualized using three-dimensional response levels.

2.5 Characterization

Field emission scanning electron microscopy (FESEM TESCAN MIRA3) was used to examine the surface structures of the produced particles. The thermo-oxidative stability of modified particles was measured by thermogravimetric analysis (TGA, TA company, US, Q600). X-ray diffraction analysis (XRD, Philips, PW1730) was also performed on the hydrophobic particles.

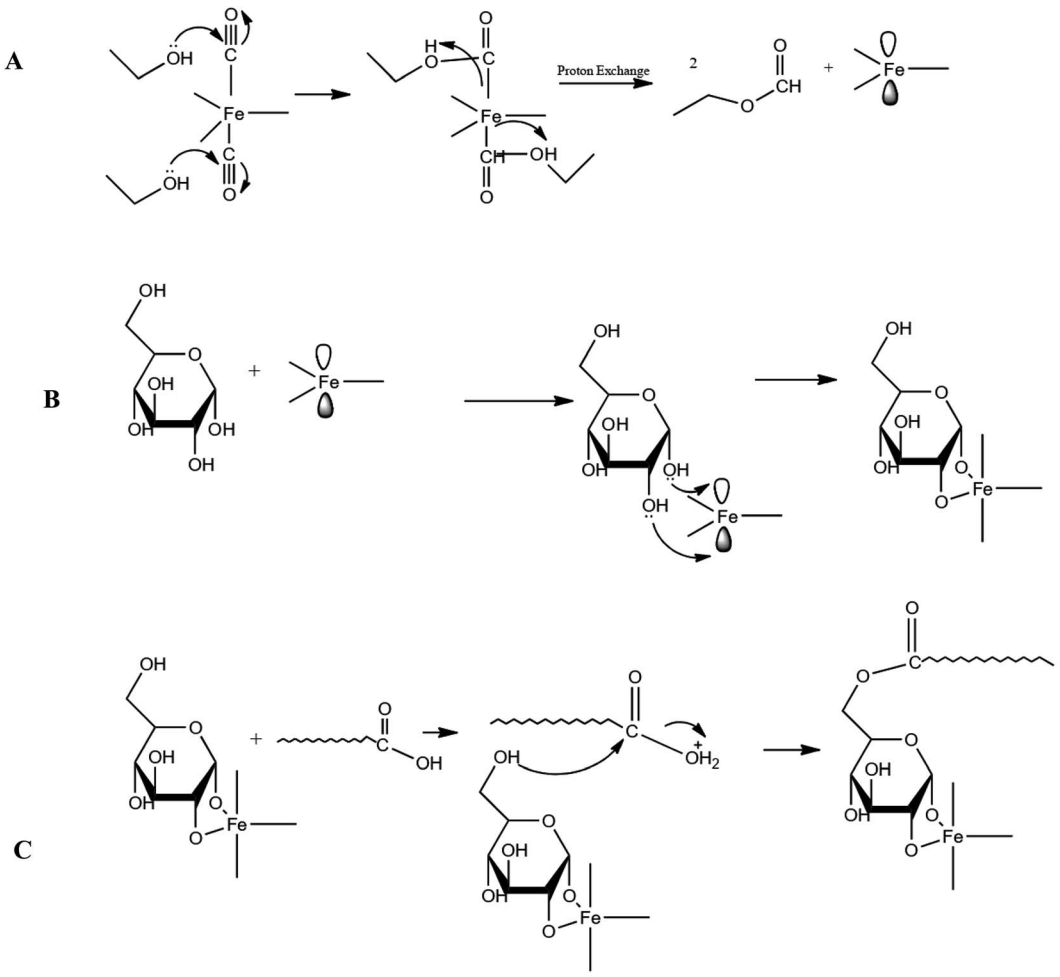

Fig. 1 The mechanism of (A) the reaction of ethanol with the Cl molecule, (B) the reaction of Fe^{2+} with glucose, (C) the reaction of Cl@G with stearic acid.

© 2022 The Author(s). Published by the Royal Society of Chemistry

Open Access Article. Published on 26 April 2022. Downloaded on 5/31/2026 3:32:46 PM.
This article is licensed under a Creative Commons Attribution-NonCommercial 3.0 Unported Licence.

Infrared spectra were obtained on an FT-IR spectrophotometer (THERMO, AVATAR). Princeton Applied Research (Vibrating Sample Magnetometer, Model no. 155) was used to investigate the magnetic characteristics of the hydrophobic particles.

2.6 Water contact angle measurement

The values of the water contact angle were measured for all modified particles using a sessile drop approach and oscillation. This method was done using a CAG-20, Jikan Co. instrument and Jikan Assistant, and Image-J software. Five microliters of the water droplets were placed on the sample and then photographed by a high-precision camera. For more accuracy, the measurement of the water contact angle was repeated five times and at the end, the average was reported. The oil contact angle was also measured in the same way.

3. Results and discussion

The synthesis was carried out according to Table 1 based on the method described in Section 2. The order of synthesis of each sample was randomly selected based on software suggestions. Runs 7 to 12 were done for repeatability tests and were operated in different orders among other runs to prevent systematic error. Fig. 1 depicts the reaction mechanism of glucose and stearic acid on the carbonyl iron particles. Some researchers have looked into a similar method mechanism.[1]

Ethanol molecules cause two orbitals of the Fe atom in the CI molecule to be empty and ready to accept electron pairs; in other words, the O atom of the OH group available in the ethanol molecule donates its electrons to make a bond with the C atom in the electrophile CO group connected to Fe. The proton of the OH group bonds to the Fe, and the Fe–CO bond becomes disconnected in this way. This happens to two CO groups of the CI molecule and thus causes two orbitals of the Fe atom to be empty and ready to accept the electron pairs of O atoms that are available in the glucose molecule. In this regard, a stable cycle with five sides is formed. It is worth mentioning that Fe bonds to two OH groups of glucose, which are on the same side. In the next step, the stearic acid carboxyl group bonds with the OH group of the glucose linked to *C* of type 1. To be more specific, the carboxyl group of stearic acid draws one proton, resulting in the formation of the OH^{2+} leaving group. The OH^{2+} species leaves the stearic acid molecule after receiving an electron pair from the stated OH group of glucose, and stearic acid binds to glucose.

The structural characterization of some modified carbonyl iron samples is depicted in Fig. 2. The carbonyl iron particles have a uniform size of about 2.3 ± 0.3 μ as shown through the image processing of the obtained FESEM image. As seen in Fig. 2A, the reaction did not occur due to the low concentration of glucose and short reaction time (run 6). Further, at low glucose concentrations, glucose and carbonyl iron reactions

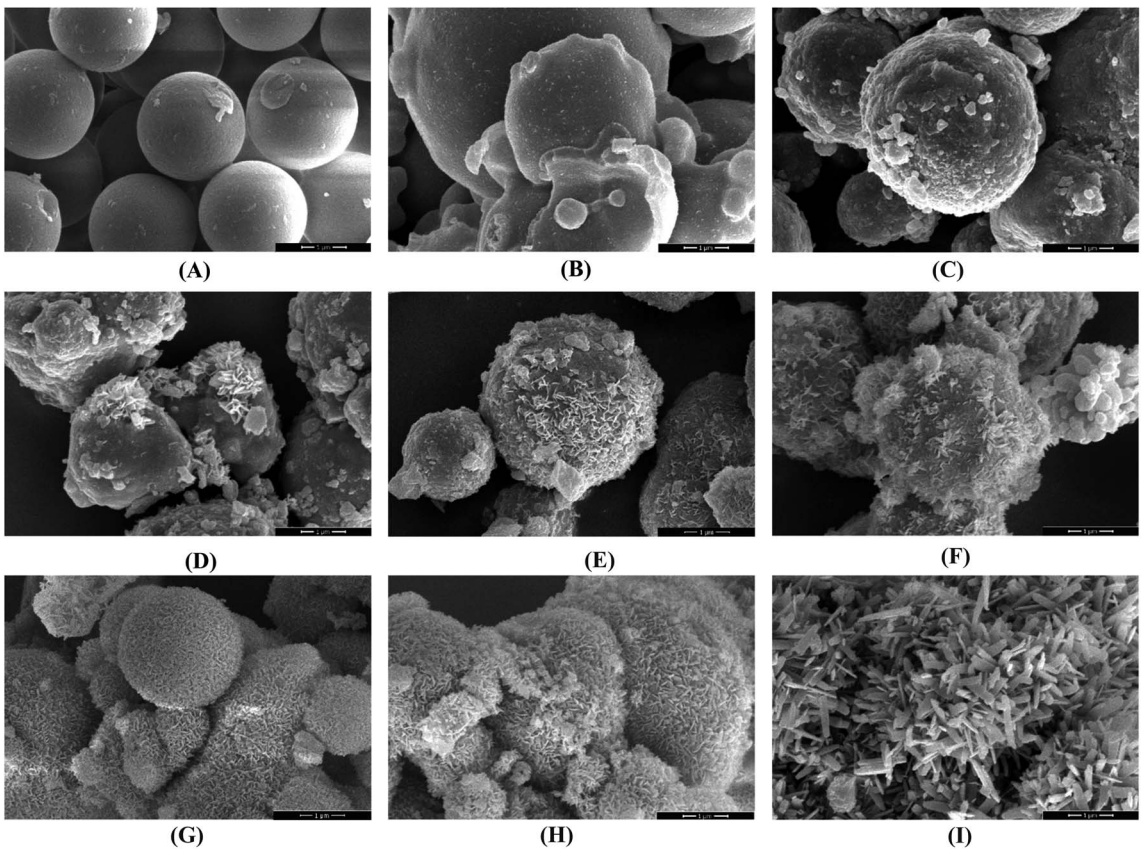

Fig. 2 FESEM images of the obtained particles under the different conditions of synthesis: A (run 6), B (run 3), C (run 1), D (run 7), E (run 19), F (run 4), G (run 14), H (run 15), I (run 5).

Open Access Article. Published on 26 April 2022. Downloaded on 5/31/2026 3:32:46 PM.
This article is licensed under a Creative Commons Attribution-NonCommercial 3.0 Unported Licence.

started to go forward over time (Fig. 2B (run 3) and 2C (run 1)). On the other hand, the temperature parameter had a negative effect on the reaction efficiency since with the increase in temperature, the growth of prickly-shaped particles decreased (Fig. 2D (run 7), Fig. 2E (run 19), and Fig. 2F (run 4)).

Eventually, the prickly shape of carbonyl iron particles grew with the reduction of temperature and elevation of the concentration of glucose and the time of the reaction (Fig. 2G (run 14), Fig. 2H (run 15), and Fig. 2I (run5)).

FESEM images in Fig. 2 were magnified twice to display the prickly shape of the particles (Fig. S1†). FESEM images (Fig. 2 and S1†) indicate that samples Fig. 2G, H, and I (run 14, 15, and 5) had better coverage than the others, as well as a more homogeneous coating of glucose and roughness of the surface of the particles. These samples had a prickly structure, and the thickness of the blades was about 10 to 100 nm. Based on the obtained results, it seems that time and glucose concentration had greater effects on the growth of the prickly shape of the particles as compared to temperature. However, more evidence is required to confirm this claim using quantitative analysis. For the quantitative assessment of the superhydrophobicity of the modified particles, the WCA values were measured using the sessile drop approach and oscillation for all synthesized particles, with the results presented in Fig. 3 and Table 2.[33]

The WCA of samples were investigated by Image-J software, with the resulting data reported in Table 2. The contact angle can be used to compare the hydrophobicity of the particles; the larger the contact angle, the more hydrophobic the particles are. As can be seen in Table 2, the contact angle did not increase due to the low concentration of glucose and short reaction time (run 6), while the contact angle was then elevated by increasing the reaction time (run 3 and 1). Overall, the WCA of modified

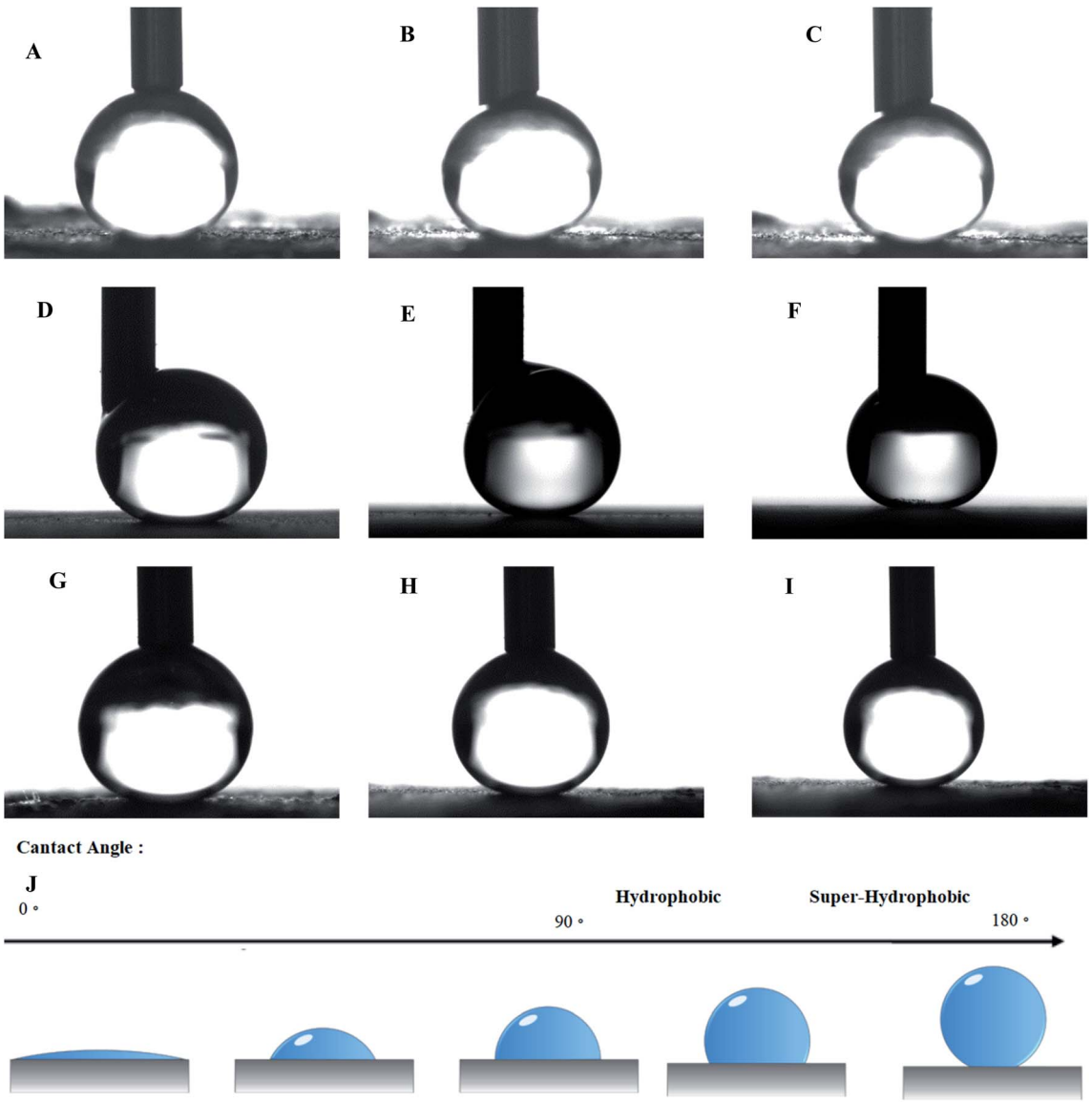

Fig. 3 The optical images of a water droplet placed on a bed of the CI @ Glucose @ Stearic acid for different samples: A (run 6), B (run 3), C (run 1), D (run 7), E (run 19), F (run 4), G (run 14), H (run 15), I (run 5) and J (the schematic of hydrophobicity based on the shape of a water droplet).

© 2022 The Author(s). Published by the Royal Society of Chemistry

Open Access Article. Published on 26 April 2022. Downloaded on 5/31/2026 3:32:46 PM.
This article is licensed under a Creative Commons Attribution-NonCommercial 3.0 Unported Licence.

Table 2 The water contact angles for all modified samples

Run	Factors: Temperature (°C)	Concentration (Mol L^{-1})	Time (hour)	Water contact angle (degree)	Contact angle hysteresis (degree)
1	160	0.5	3	157.04 ± 0.50	3 ± 1
2	170	0.25	2	153.01 ± 0.40	3 ± 1
3	170	0.25	4	155.05 ± 0.50	3 ± 1
4	170	0.75	2	163.02 ± 0.30	2 ± 1
5	170	0.75	4	169.71 ± 0.20	0 ± 1
6	180	0	3	150.01 ± 0.50	5 ± 1
7–12	180	0.5	3	160.00 ± 0.50	2 ± 1
13	180	0.5	1	156.98 ± 0.40	3 ± 1
14	180	0.5	5	164.01 ± 0.20	2 ± 1
15	180	1	3	167.99 ± 0.30	1 ± 1
16	190	0.25	2	152.50 ± 0.40	5 ± 1
17	190	0.25	4	154.07 ± 0.50	4 ± 1
18	190	0.75	2	158.01 ± 0.20	3 ± 1
19	190	0.75	4	163.03 ± 0.30	2 ± 1
20	200	0.5	3	154.00 ± 0.50	3 ± 1

Table 3 The ANOVA results based on the Design Expert Software[a]

Source	Sum of squares	Degree of freedoms	Mean square	*F*-value	*P*-value
Model	488.41	9	54.27	123.73	<0.0001
T	23.06	1	23.06	52.59	<0.0001
C	353.53	1	353.53	806.05	<0.0001
t	53.33	1	53.33	121.58	<0.0001
TC	13.03	1	13.03	29.71	0.0003
Tt	0.6105	1	0.6105	1.39	0.2654
Ct	8.43	1	8.43	19.21	0.0014
T^2	32.98	1	32.98	75.20	<0.0001
C^2	1.84	1	1.84	4.19	0.0679
t^2	0.2754	1	0.2754	0.6279	0.4465
Residual	4.39	10	0.4386		
Lack of fit	4.39	5	0.8772		
Pure error	0.0000	5	0.0000		
Fit statistics					
Std. Dev	0.6623		Adjusted R^2		0.9831
Mean	158.91		Predicted R^2		0.9261
C.V. %	0.4168		Adequate precision	41.5918	
R^2	0.9911				

[a] A *P*-value of less than 0.0001 implies that the model was significant. Accordingly, the terms *Tt*, t^2, and C^2, which are the interaction effect of two *T* and *t* parameters and the square effect of each *t* and *C* parameter, were omitted.

particles increased with the decrease in temperature and increase in the concentration of glucose and the time of the reaction (run 14, 15, and 5).

Generally, there are two essential factors in making CI particles superhydrophobic: high surface roughness and low surface energy. The high roughness of the surface makes more cavities throughout the surface, which become filled with air and make less of the surface contact with water. On the other hand, the low surface energy increases the hydrophobicity by reducing the coherence of the water droplet.[34–36] In this regard, glucose molecules were used to boost the roughness of the CI particles, and stearic acid molecules were used to reduce the surface energy. As can be seen in Fig. 2, 3 and Table 2, the optimized parameters that can increase the prickly shape of the modified CI particles can also mount the contact angle of the particles.

Also, the contact angle hysteresis (CAH) was measured and reported in Table 2 for all samples. Finally, the oil contact angle was measured for all particles, which was zero.

3.1 Polynomial regression model and analysis of variance (ANOVA)

In the experimental design software, a model predicting the effect of different parameters was represented. The ANOVA analysis was then used to determine whether each variable of the model attributed to each evaluating parameter is meaningful in the

Open Access Article. Published on 26 April 2022. Downloaded on 5/31/2026 3:32:46 PM.
This article is licensed under a Creative Commons Attribution-NonCommercial 3.0 Unported Licence.

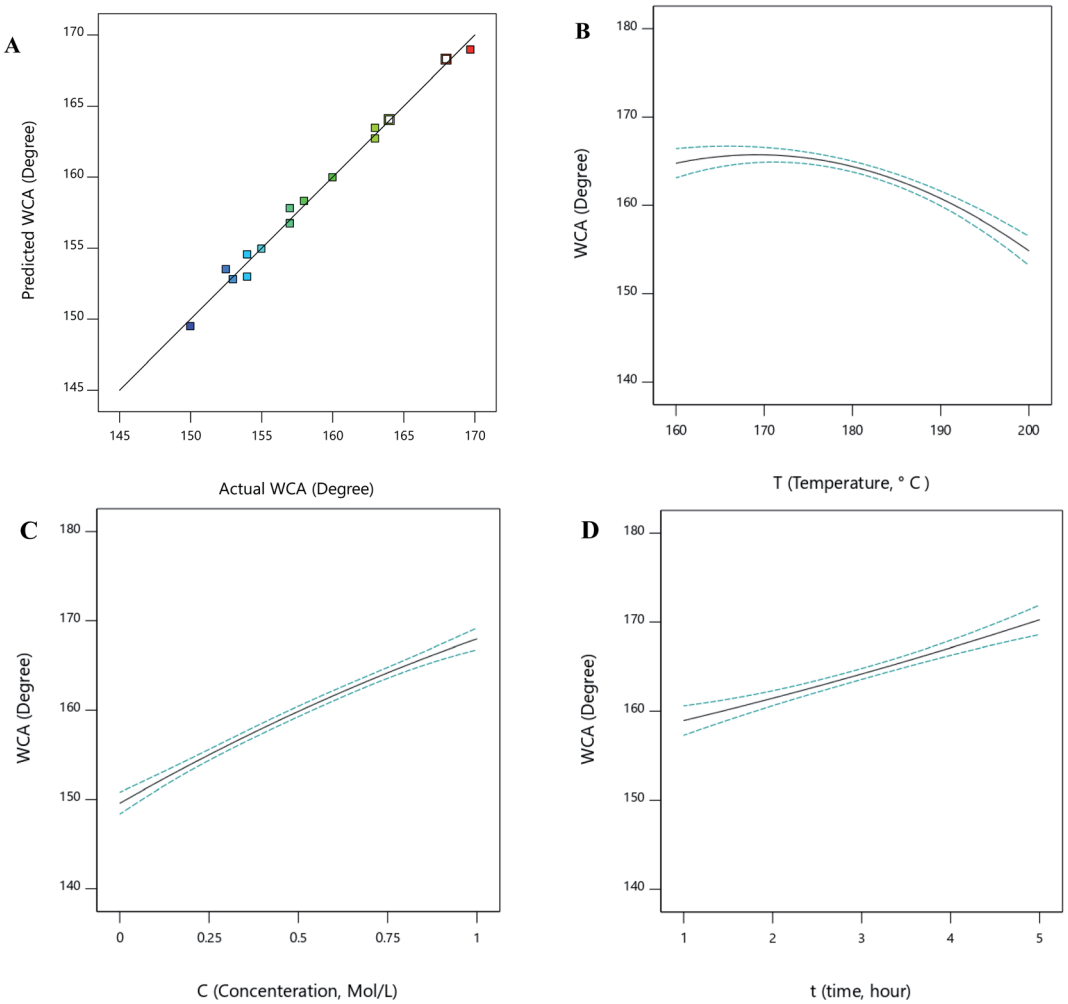

Fig. 4 The predicted *vs.* actual data for the water contact angle (A) and the effects of different parameters on WCA, (B) temperature, (C) concentration, (D) time.

model or not. In other words, the ANOVA method recognizes which parameter has a significant effect on the target response. According to the experimental design method and the polynomial model (eqn (1)), the results are reported in Table 3.

In this case, T (temperature), C (concentration), t (time), TC, Ct, and T^2 terms are significant. More specifically, TC, Ct, and T^2 terms are the interaction effects of two T and C parameters as well as C and t parameters, respectively. The T^2 term, on the other hand, shows the square effect of parameter T. Based on the F-value, the importance of variables is as follows:

$$C > t > T \quad (2)$$

As shown in Fig. 4A, the experimental data fit the regression line where the coefficient of determination is 0.9911. The model predicted by the Design-Expert software is shown in eqn (3). Note that the insignificant terms have been omitted from the equation.

$$\text{Contact angle} = -259.24244 + 4.34129T + 102.70295C + 4.11767t - 0.510500\text{T} \times C + 4.10500\, C \times t - 4.32545C^2 \quad (3)$$

3.2 The impact of various parameters on the contact angle

According to the results provided by the Design-Expert software, the one-factor plots related to each parameter of temperature, concentration, and time can be seen in Fig. 4B–D. From the figures, the WCA increased with increasing concentration and time. WCA was also diminished by the temperature elevation.

The interaction plots related to the interaction parameters of temperature-concentration, concentration–time, and temperature–time can be seen in Fig. 5.

As depicted in Fig. 5A and 5B, the contact angle increased with the elevation of the glucose concentration due to the creation of a prickly-shaped layer on the carbonyl iron surface. This increase causes greater surface hydrophobicity and increases the contact angle. The elevation of the temperature first increases the contact angle and then decreases it (Fig. 5A), suggesting that at temperatures below 180, the contact angle increased sharply. It also shows that at low temperatures, increasing the concentration had a greater effect on the contact angle.

As shown in Fig. 5B and 5C, increasing the time leads to a greater contact angle. In this regard, blades need to have

© 2022 The Author(s). Published by the Royal Society of Chemistry

Open Access Article. Published on 26 April 2022. Downloaded on 5/31/2026 3:32:46 PM.
This article is licensed under a Creative Commons Attribution-NonCommercial 3.0 Unported Licence.

enough time to grow and increase the contact angle. Furthermore, at low concentrations, the blades did not grow significantly since there were insufficient reactants to be consumed in the reaction. As a result, the effect of the concentration parameter on the contact angle has not been significant within low concentration ranges. Fig. 5C shows that the contact angle value remained constant as the time increased beyond 3 hours. According to Fig. 5, the optimal ranges for temperature, concentration, and time are 160 to 180 °C, 0.5 to 1 Mol L^{-1}, and 3 to 5 hours, respectively.

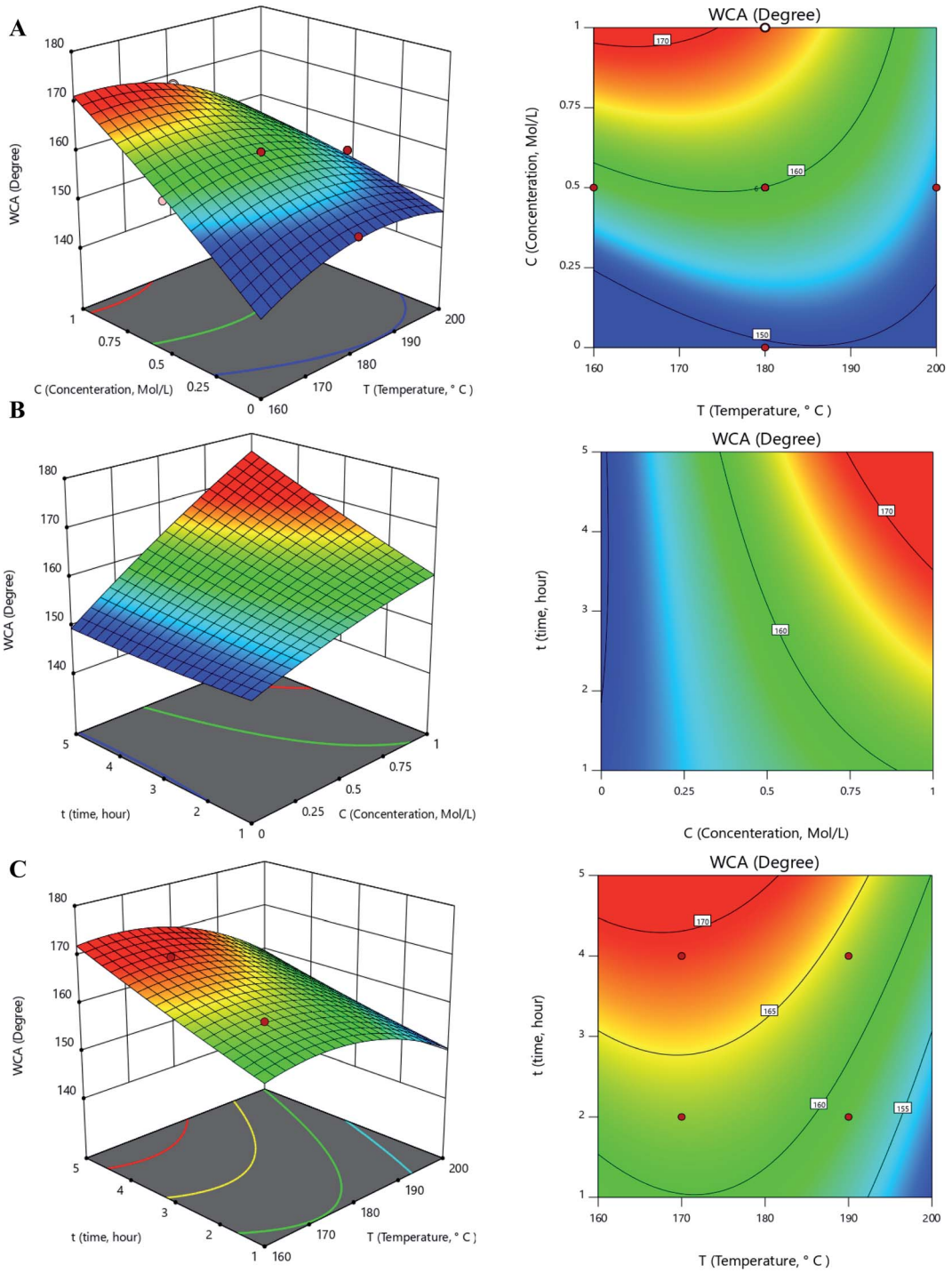

Fig. 5 3D response surface and contour plot of WCA: (A) the interaction between concentration and temperature at a constant time, $t = 3$ h. (B) The interaction between concentration and time at a constant temperature, $T = 180$ °C. (C) The interaction between temperature and time at a constant concentration, $C = 0.5$ Mol/L^{-1}.

Open Access Article. Published on 26 April 2022. Downloaded on 5/31/2026 3:32:46 PM.
This article is licensed under a Creative Commons Attribution-NonCommercial 3.0 Unported Licence.

3.3. Optimization of the effects of different parameters on WCA and validation results

The optimization was performed using the Design-Expert software. Many local optimal points were suggested, the best of which were the concentration, time, and temperature of 170 °C, 0.75 Mol L^{-1}, and 4 hours, respectively. In this regard, the contact angle value with the optimum amount of mentioned parameters was predicted to be 168.954°. The experiment with the best parameter values was repeated three times and the experimental WCA was obtained as 168.50° with a relative standard deviation (RSD) of 0.6%.

3.4. Characterization of an optimized sample

The results of the FESEM, FT-IR, XRD, TGA, and VSM analyses for the sample obtained using the optimum amount of parameters are given as follows. In the optimal sample, due to sufficient time, appropriate concentration and temperature, the blades grew to 100 nm (FESEM image in Fig. 6A). The roughness due to glucose and low surface energy using stearic acid dramatically increased the hydrophobicity (increased contact angle up to 168.954° for the optimum sample). The surface roughness created on the surface of the iron carbonyl particles created more cavities on the surface that were filled with air and reduced the surface contact with water. On the other hand, low surface energy increased the hydrophobicity by reducing the adhesion of water droplets. Therefore, the synthesized rough micro-nano structures had maximum hydrophobicity.

The Fourier-transform infrared (FT-IR) spectra of the optimized sample confirmed the presence of the functional groups related to stearic acid and glucose coated on the CI particles. The FT-IR spectra of carbonyl iron and the carbonyl iron modified by glucose and stearic acid are displayed in Fig. 6C. The coordination of Fe^{2+} in CI with the carbonyl group of glucose caused the peak related to the C=O group to appear at a lower wavenumber. As a result, in the FT-IR spectrum of CI@G, the peak of the C=O carbonyl group shifted from 1632 cm^{-1} to 1617 cm^{-1} as compared to CI particles. The peak for the C=O group was observed at 1700 cm^{-1} in the FT-IR spectrum of stearic acid, which was also evident in the FT-IR

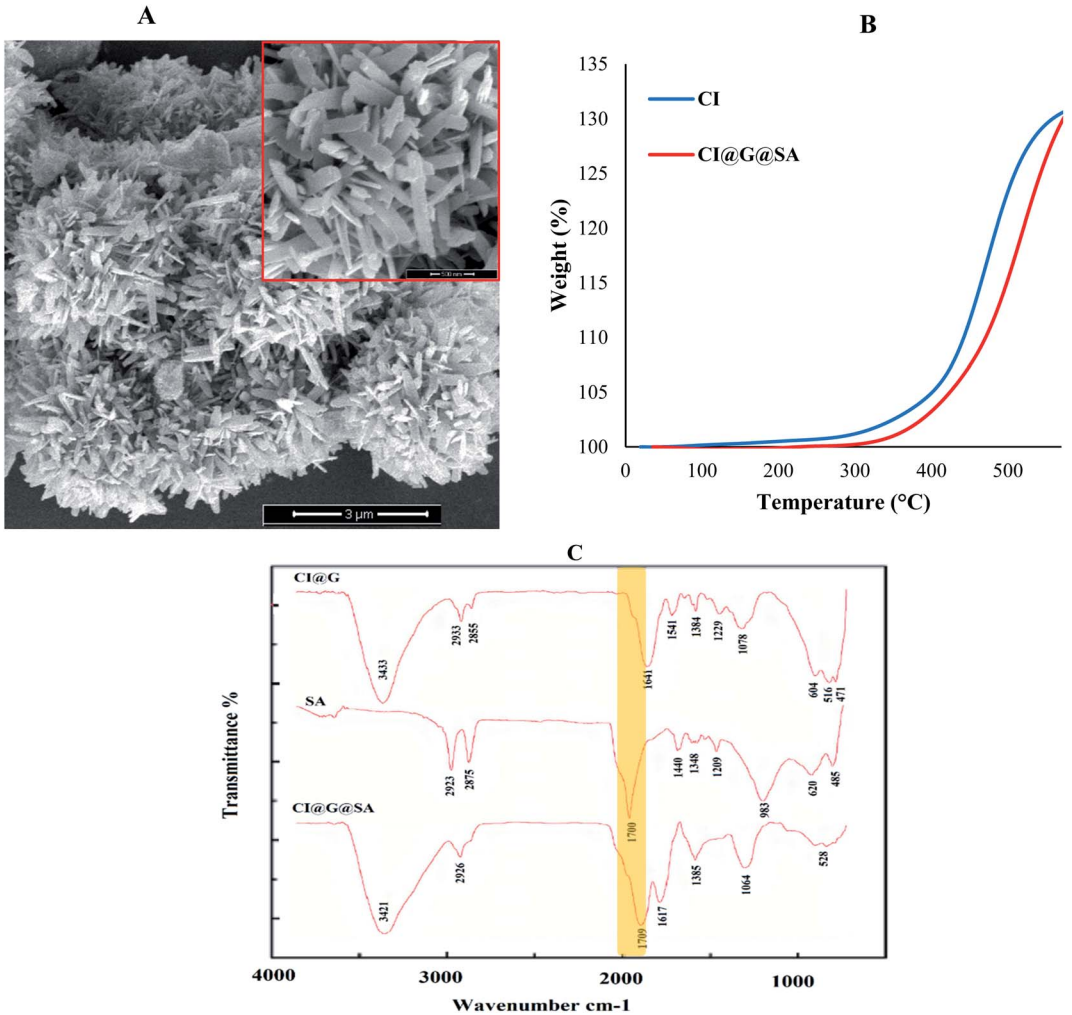

Fig. 6 (A) FESEM image of the optimum sample. (B) TGA curve of carbonyl iron particles before and after modification. (C) FT-IR spectra of CI@G: carbonyl iron particles modified with glucose, SA: stearic acid and CI@G@SA: carbonyl iron particles modified with glucose and stearic acid.

© 2022 The Author(s). Published by the Royal Society of Chemistry

Open Access Article. Published on 26 April 2022. Downloaded on 5/31/2026 3:32:46 PM.
This article is licensed under a Creative Commons Attribution-NonCommercial 3.0 Unported Licence.

spectrum of CI@G@SA acid. As a result, the existence of peaks related to the carbonyl groups of stearic acid and glucose revealed that glucose and stearic acid were reacting on the CI particles.

The thermogravimetric analysis (TGA) curves of carbonyl iron particles before and after modification are shown in Fig. 6B. As can be seen, the Fe of the carbonyl iron particles was oxidized between 300 and 400 °C due to iron oxide formation (FeO and Fe_3O_4). The degradation of CI@Gl@SA particles occurred due to the coating of CI with SA and G. TGA of CI@Gl@SA confirmed the chemical bond between CI, glucose, and stearic acid since through the temperature increase, the sample weight increased due to the oxidation process. If CI@Gl@SA contained volatile compounds physically bonded to each other, the TGA curve would show a decrease through the loss of these components.[37,38]

Surface modification of carbonyl iron particles at high temperatures may alter the crystal structure or cause the surface of the particles to oxidize. The XRD patterns of CI, CI@G, and CI@G@SA are presented in Fig. 7A. The XRD results show that there was no peak related to iron oxide (the iron oxide peak appears at approximately 18.3°, 30.1°, and 35.4°). However, the 2θ of 44° (assigned to (110)) and 65° (assigned to (200)) related to the Fe peaks in the synthesized sample, were observed in the XRD pattern. Therefore, oxidation did not occur during the synthesis process.[39,40] It was found that all the diffraction peaks were well indexed with the ferrite.

VSM was used to measure the magnetic characteristics of the modified particles at room temperature. Fig. 7B shows the magnetic plot of the CI, CI@G, and CI@G@SA particles. The magnetic curve is a graph obtained when the magnetization of particles (emu g^{-1}) is plotted *versus* the applied magnetic field (Oersted or Oe). As can be seen in Fig. 7B, the magnetization of particles increases to a point and then reaches a saturation point where no change in the magnetic field can increase the magnetization property of the particles. Overall, when the CI particles were modified by nonmagnetic materials, the magnetic property decreased. With this explanation, the saturation magnetization (Ms) for CI, CI@G, and CI@G@SA were 210, 199, 189 emu g^{-1}, respectively. The absence of magnetic

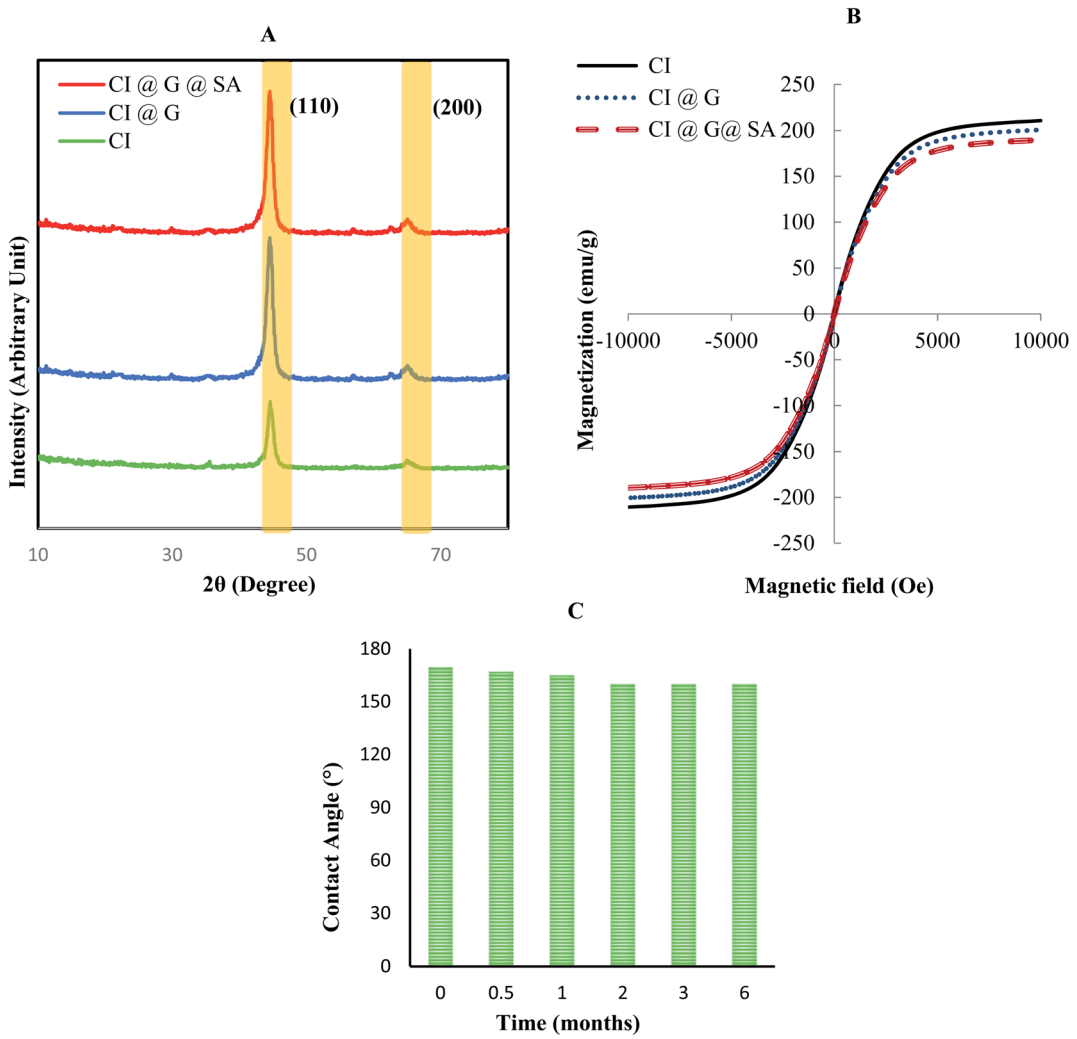

Fig. 7 (A) XRD pattern of carbonyl iron particles before and after modification. (B) VSM plot for modified carbonyl iron particles. (C) Stability of the particle over time.

Open Access Article. Published on 26 April 2022. Downloaded on 5/31/2026 3:32:46 PM.
This article is licensed under a Creative Commons Attribution-NonCommercial 3.0 Unported Licence.

residue in the particles modified with glucose and stearic acid indicates that the particles were well modified and there was no aggregation of particles after modification. The slight decrease in the magnetic saturation of these particles is due to the non-magnetic modification of these particles.[41]

Fig. 7B shows that Ms values of modified CI particles are close to the CI particles without modification (10% difference), which confirmed the high magnetization of the modified particles. The high magnetic properties of these particles, despite the modification, are an excellent property for controlling the process of collecting contaminants. The stability of modified particles (optimal sample) was measured over time by contact angle for 6 months. Fig. 7C shows the water contact angle of the optimum sample at a different time point. As can be seen, the superhydrophobicity of this sample did not change over time and this fact indicated that the structure of the particle hydrophobicity did not change over time.

4. Conclusions

In this paper, the parameters affecting the synthesis of CI@G@SA particles were optimized to increase the hydrophobicity of the particles. In this regard, the five-level experiment by the full Central Composite Design was used in the Response Surface Methodology by the Design-Expert software (Ver.11.0.0) to optimize the hydrophobicity of the particles. To achieve the maximum hydrophobicity, 20 experiments were selected based on experimental design to study the effects of glucose concentration, temperature, and reaction time parameters.

The qualitative and quantitative analyses were conducted on the synthesized samples to confirm the synthesis process. The qualitative analysis included Field Emission Scanning Electron Microscopy (FESEM), and the quantitative analysis included the measurement of the contact angles of all samples using a sessile drop approach and oscillation. The results showed that the increase in glucose concentration and time initially caused more surface roughness of the particles and increased the contact angle, and in the end, the increase of the glucose concentration and time did not affect the blade growth on the particles, or the contact angle. The temperature also first caused an increase in the blade growth and then led to a sharp decrease in the blades and the contact angle. Software optimization showed that the best values of the concentration, temperature, and time parameters to achieve the maximum blade growth and hydrophobicity were 170 °C, 0.75 Mol L^{-1}, and 4 hours, respectively, which resulted in the contact angle of 168.954°. The experiment with the best parameter values was repeated three times and the experimental WCA of 168.50° was obtained with a relative standard deviation (RSD) of 0.6%.

X-ray diffraction analysis(XRD) was performed on the optimum superhydrophobic particles and the results showed that there was no peak related to iron oxide and thus, the oxidation reaction did not occur during the synthesis process. Infrared spectra were also obtained using an FT-IR spectrophotometer. The FT-IR spectrum of the synthesized particles confirmed the presence of the functional groups of glucose (C=O, C–O, and OH) and stearic acid (COOH and CH_2) bonded to CI. The thermogravimetric analysis (TGA) showed that the CI was degraded between 300 and 400 °C due to iron oxide formation. Also, the oxidization of CI@G@SA occurred due to the chemical bond between CI with glucose, and stearic acid. After that, a Vibrating Sample Magnetometer (VSM) was used to determine the magnetic characteristics of the hydrophobic particles. The results of the VSM analysis showed that the values of the magnetic saturation of CI, CI@G, and CI@G@SA were 210, 199, 189 emu g^{-1}, respectively. The superhydrophobic particles showed good stability after the sample was stored and the results showed that the superhydrophobicity of the optimal sample did not change over 6 months. All the results obtained by different analyses showed that the modified particles had good superhydrophobicity and, therefore, the application of these particles in the oil-water separation approach is worth studying due to their high level of superhydrophobicity.

Author contributions

Yahya Rabbani: experimental design, synthesis process, result and discussion, write and edit of paper. Mojtaba Shariaty-Niassar: supervision, result and discussion, review, and edit of the paper. Seyyed Ali Seyyed Ebrahimi: co-supervision, review, and edit of the paper.

Conflicts of interest

There are no conflicts to declare.

Acknowledgements

Financial Support (Grant No. 99020988) from the Iran National Science Foundation is gratefully acknowledged.

References

1 Y. Rabbani, M. Shariaty-Niassar and S. A. S. Ebrahimi, The effect of superhydrophobicity of prickly shape carbonyl iron particles on the oil-water adsorption, *Ceram. Int.*, 2021, **47**, 28400–28410, DOI: **10.1016/j.ceramint.2021.06.257**.

2 Y. Rabbani, M. Shariaty-Niassar and S. A. Seyyedebrahimi, An Investigation of the Effects of Dopamine on Hydrophobicity of Carbonyl Iron Particles with Stearic Acid, *Iran. J. Chem. Eng.*, 2020, **17**, 49–59, DOI: **10.22034/ijche.2020.129383**.

3 H. Shayesteh, R. Norouzbeigi and A. Rahbar-Kelishami, Hydrothermal facile fabrication of superhydrophobic magnetic nanospiky nickel wires: Optimization *via* statistical design, *Surf. Interfaces*, 2021, **26**, DOI: **10.1016/j.surfin.2021.101315**.

4 J. Yong, F. Chen, Q. Yang, H. Bian, G. Du, C. Shan, J. Huo, Y. Fang and X. Hou, Oil-water separation: A gift from the desert, *Adv. Mater. Interfaces*, 2016, **3**, 1–7, DOI: **10.1002/admi.201500650**.

5 M. Ge, C. Cao, J. Huang, X. Zhang, Y. Tang, X. Zhou, K. Zhang, Z. Chen and Y. Lai, Rational design of materials interface at nanoscale towards intelligent oil-water

© 2022 The Author(s). Published by the Royal Society of Chemistry

Open Access Article. Published on 26 April 2022. Downloaded on 5/31/2026 3:32:46 PM. This article is licensed under a Creative Commons Attribution-NonCommercial 3.0 Unported Licence.

separation, *Nanoscale Horiz.*, 2018, **3**, 235–260, DOI: 10.1039/c7nh00185a.

6 S. Parvate, P. Dixit and S. Chattopadhyay, Superhydrophobic Surfaces: Insights from Theory and Experiment, *J. Phys. Chem. B*, 2020, **124**, 1323–1360, DOI: 10.1021/acs.jpcb.9b08567.

7 X. Tang, C. Shen, W. Zhu, S. Zhang, Y. Xu, Y. Yang, M. Gao and F. Dong, A facile procedure to modify filter paper for oil-water separation, *RSC Adv.*, 2017, **7**, 30495–30499, DOI: 10.1039/c7ra03754f.

8 Y. Rabbani and O. Tavakoli, Experimental Study on Stability of Magnetorheological Fluid by Using of Fe_3O_4/Cellulose Nanoparticles, *Amirkabir J. Mech. Eng.*, 2021, **52**, 689–692, DOI: 10.22060/mej.2019.16403.6359.

9 L. Dashairya, G. M and P. Saha, Synergistic effect of Zr/Cl dual-ions mediated pyrrole polymerization and development of superhydrophobic melamine sponges for oil/water separation, *Colloids Surf., A*, 2020, **599**, 124877, DOI: 10.1016/j.colsurfa.2020.124877.

10 J. Du, C. Zhang, H. Pu, Y. Li, S. Jin, L. Tan, C. Zhou and L. Dong, HKUST-1 MOFs decorated 3D copper foam with superhydrophobicity/superoleophilicity for durable oil/water separation, *Colloids Surf., A*, 2019, **573**, 222–229, DOI: 10.1016/j.colsurfa.2019.04.064.

11 M. Cvek, R. Moucka, M. Sedlacik and V. Pavlinek, Electromagnetic, magnetorheological and stability properties of polysiloxane elastomers based on silane-modified carbonyl iron particles with enhanced wettability, *Smart Mater. Struct.*, 2017, **26**, 105003, DOI: 10.1088/1361-665X/aa85c5.

12 K. L. Pickering, S. Raa Khimi and S. Ilanko, The effect of silane coupling agent on iron sand for use in magnetorheological elastomers Part 1: Surface chemical modification and characterization, *Composites, Part A*, 2015, **68**, 377–386, DOI: 10.1016/j.compositesa.2014.10.005.

13 B. Singh, S. Kumar, B. Kishore and T. N. Narayanan, Magnetic scaffolds in oil spill applications, *Environ. Sci.: Water Res. Technol.*, 2020, **6**, 436–463, DOI: 10.1039/C9EW00697D.

14 S. Ko, E. S. Kim, S. Park, H. Daigle, T. E. Milner, C. Huh, M. V. Bennetzen and G. A. Geremia, Amine functionalized magnetic nanoparticles for removal of oil droplets from produced water and accelerated magnetic separation, *J. Nanopart. Res.*, 2017, **19**, DOI: 10.1007/s11051-017-3826-6.

15 L. Liu, X. Pu, H. Tao, K. Chen, W. Guo, D. Luo and Z. Ren, Pickering emulsion stabilized by organoclay and intermediately hydrophobic nanosilica for high-temperature conditions, *Colloids Surf., A*, 2021, **610**, 125694, DOI: 10.1016/j.colsurfa.2020.125694.

16 N. P. Holley, J. G. Lee, K. T. Valsaraj and B. Bharti, Synthesis and characterization of ZEin-based Low Density Porous Absorbent (ZELDA) for oil spill recovery, *Colloids Surf., A*, 2021, **614**, 126148, DOI: 10.1016/j.colsurfa.2021.126148.

17 H. You, G. Y. Shangkum, P. Chammingkwan and T. Taniike, Surface wettability switching of a zeolitic imidazolate framework-deposited membrane for selective efficient oil/water emulsion separation, *Colloids Surf., A*, 2021, **614**, 126204, DOI: 10.1016/j.colsurfa.2021.126204.

18 M. Shi, R. Huang, W. Qi, R. Su and Z. He, Synthesis of superhydrophobic and high stable Zr-MOFs for oil-water separation, *Colloids Surf., A*, 2020, **602**, 125102, DOI: 10.1016/j.colsurfa.2020.125102.

19 Y. Cai, Q. Zhao, X. Quan, W. Feng and Q. Wang, Fluorine-free and hydrophobic hexadecyltrimethoxysilane-TiO2 coated mesh for gravity-driven oil/water separation, *Colloids Surf., A*, 2020, **586**, 124189, DOI: 10.1016/j.colsurfa.2019.124189.

20 S. Rasouli, N. Rezaei, H. Hamedi, S. Zendehboudi and X. Duan, *Design, Fabrication, and Characterization of a Facile Superhydrophobic and Superoleophilic Mesh-Based Membrane for Selective Oil-Water Separation*, Chemical Engineering Science. (2020) p. 116354. DOI: 10.1016/j.ces.2020.116354.

21 Z. Wu, W. Deng, W. Zhou and J. Luo, Novel magnetic polysaccharide/graphene oxide @Fe_3O_4 gel beads for adsorbing heavy metal ions, *Carbohydr. Polym.*, 2019, **216**, 119–128, DOI: 10.1016/j.carbpol.2019.04.020.

22 B. Zhang, S. Chen, H. Luo, B. Zhang, F. Wang and J. Song, Porous amorphous powder form phase-selective organogelator for rapid recovery of leaked aromatics and spilled oils, *J. Hazard. Mater.*, 2020, **384**, 31414, DOI: 10.1016/j.jhazmat.2019.121460.

23 H. Shayesteh, R. Norouzbeigi and A. Rahbar-Kelishami, Evaluation of superhydrophobicity of chemical-resistant magnetic spiky nickel nanowires grafted with silane coupling agent for highly efficient oil/water separation, *Surf. Interfaces*, 2022, **28**, DOI: 10.1016/j.surfin.2021.101685.

24 H. Shayesteh, A. Rahbar-Kelishami and R. Norouzbeigi, Superhydrophobic/superoleophilic micro/nanostructure nickel particles for oil/water mixture and emulsion separation, *Ceram. Int.*, 2022, DOI: 10.1016/j.ceramint.2021.12.320.

25 G. Simonsen, M. Strand and G. Øye, Potential applications of magnetic nanoparticles within separation in the petroleum industry, *J. Pet. Sci. Eng.*, 2018, **165**, 488–495, DOI: 10.1016/j.petrol.2018.02.048.

26 C. Duan, T. Zhu, J. Guo, Z. Wang, X. Liu, H. Wang, X. Xu, Y. Jin, N. Zhao and J. Xu, Smart enrichment and facile separation of oil from emulsions and mixtures by superhydrophobic/superoleophilic particles, *ACS Appl. Mater. Interfaces*, 2015, **7**, 10475–10481, DOI: 10.1021/acsami.5b01901.

27 Q. Zhu, F. Tao and Q. Pan, Fast and selective removal of oils from water surface *via* highly hydrophobic core-shell Fe_2O_3@C nanoparticles under magnetic field, *ACS Appl. Mater. Interfaces*, 2010, **2**, 3141–3146, DOI: 10.1021/am1006194.

28 J. Maroofi, S. H. Hashemabadi and Y. Rabbani, Investigation of the chain formation effect on thermal conductivity of magnetorheological fluids, *J. Thermophys. Heat Transfer*, 2020, **34**, DOI: 10.2514/1.T5656.

29 A. E. Pourshayan, A. Rabbani, S. Farahani, Y. Rabbani, H. Ahmadi Danesh Ashtiani, M. Shariat, M. Gholi Nejad and A. A. Emami Satlooand *Modeling and Simulation of*

Open Access Article. Published on 26 April 2022. Downloaded on 5/31/2026 3:32:46 PM.
This article is licensed under a Creative Commons Attribution-NonCommercial 3.0 Unported Licence.

Magnetorheological Fluid Sleeve Valve, (n.d.). DOI: 10.22034/ijche.2021.131248.

30 M. Shirvani and Y. Rabbani, *The Properties and Parameters Needed of The Magnetorheological Fluid for Use in the Intelligent Damper of the Vehicle Suspension System*, Nashrieh Shimi va Mohandesi Shimi Iran. (2019). https://www.nsmsi.ir/article_36132.html.

31 C. Duan, T. Zhu, J. Guo, Z. Wang, X. Liu, H. Wang, X. Xu, Y. Jin, N. Zhao and J. Xu, Smart enrichment and facile separation of oil from emulsions and mixtures by superhydrophobic/superoleophilic particles, *ACS Appl. Mater. Interfaces*, 2015, **7**, 10475–10481, DOI: 10.1021/acsami.5b01901.

32 H. Yang, S. Wang, W. Zhang, J. Wu, S. Yang, D. Yu, X. Wu, Y. Sun and J. Wang, Rapid demulsification of pickering emulsions triggered by controllable magnetic field, *Sci. Rep.*, 2020, **10**, DOI: 10.1038/s41598-020-73551-w.

33 H. Xie, Z. Wu, Z. Wang, J. Lu, Y. Li, Y. Cao and H. Cheng, Facile fabrication of acid-resistant and hydrophobic Fe_3O_4@SiO_2@C magnetic particles for valid oil-water separation application, *Surf. Interfaces*, 2020, **21**, 100651, DOI: 10.1016/j.surfin.2020.100651.

34 H. J. Chen, C. Yang, T. Hang, G. Liu, J. Wu, D. an Lin, A. Zhang, Y. Li, B. ru Yang and X. Xie, Nanospikes-mediated Anomalous Dispersities of Hydropobic Micro-objects and their Application for Oil Emulsion Cleaning, *Sci. Rep.*, 2018, **8**, 1–10, DOI: 10.1038/s41598-018-30339-3.

35 Y. Ouyang, J. Zhao, R. Qiu, S. Hu, Y. Zhang and P. Wang, Bioinspired superhydrophobic and oil-infused surface: Which is the better choice to prevent marine biofouling?, *Colloids Surf., A*, 2018, **559**, 297–304, DOI: 10.1016/j.colsurfa.2018.09.060.

36 N. Michael and B. Bhushan, Hierarchical roughness makes superhydrophobic states stable, *Microelectron. Eng.*, 2007, **84**, 382–386, DOI: 10.1016/j.mee.2006.10.054.

37 S. Y. Kim, S. H. Kwon, Y. D. Liu, J. S. Lee, C. Y. You and H. J. Choi, Core–shell-structured cross-linked poly(glycidyl methacrylate)-coated carbonyl iron microspheres and their magnetorheology, *J. Mater. Sci.*, 2014, **49**, 1345–1352, DOI: 10.1007/s10853-013-7818-3.

38 M. Mrlík, M. Ilčíková, M. Cvek, V. Pavlínek, A. Zahoranová, Z. Kroneková and P. Kasak, Carbonyl iron coated with a sulfobetaine moiety as a biocompatible system and the magnetorheological performance of its silicone oil suspensions, *RSC Adv.*, 2016, **6**, 32823–32830, DOI: 10.1039/c6ra03919g.

39 Y. Gu, M. Qin, Z. Cao, B. Jia, X. Wang and X. Qu, Effect of Glucose on the Synthesis of Iron Carbide Nanoparticles from Combustion Synthesis Precursors, *J. Am. Ceram. Soc.*, 2016, **99**, 1443–1448, DOI: 10.1111/jace.14117.

40 K. Sugimura, Y. Miyajima, M. Sonehara, T. Sato, F. Hayashi, N. Zettsu, K. Teshima and H. Mizusaki, Formation of high electrical-resistivity thin surface layer on carbonyl-iron powder (CIP) and thermal stability of nanocrystalline structure and vortex magnetic structure of CIP, *AIP Adv.*, 2016, **6**, DOI: 10.1063/1.4944705.

41 A. Taufiq, R. E. Saputro, Sunaryono, Y. A. Hariyanto, N. Hidayat, A. Hidayat, N. Mufti and H. Susanto, Mujamilah, Functional Group and Magnetic Properties of Fe3O4 Ferrofluids: The Impact of Dispersion Agent Composition, in: *Journal of Physics: Conference Series*, Institute of Physics Publishing, 2018. https://doi.org/DOI: 10.1088/1742-6596/1093/1/012010.

© 2022 The Author(s). Published by the Royal Society of Chemistry